

Optical absorption and carrier multiplication at graphene edges in a magnetic fieldFriedemann Queisser^{1,2}, Sascha Lang,^{1,3} and Ralf Schützhold^{1,2}¹*Helmholtz-Zentrum Dresden-Rossendorf, Bautzner Landstraße 400, 01328 Dresden, Germany*²*Institut für Theoretische Physik, Technische Universität Dresden, 01062 Dresden, Germany*³*Fakultät für Physik, Universität Duisburg-Essen, Lotharstraße 1, 47057 Duisburg, Germany*

(Received 19 December 2022; revised 19 June 2023; accepted 26 June 2023; published 7 July 2023)

We study the optical absorption at graphene edges in a perpendicular magnetic field and the subsequent charge carrier multiplication via inelastic Auger scattering. For the latter, we identify exact and approximate selection rules and give estimates for the generated edge current. This permits an understanding of the experimentally observed photoresponse in suspended graphene.

DOI: [10.1103/PhysRevB.108.045403](https://doi.org/10.1103/PhysRevB.108.045403)**I. INTRODUCTION**

Graphene offers a large mean free path, a high charge carrier mobility [1–3], and a broad absorption bandwidth [4], which makes it a promising candidate for optoelectronic applications [5–7]. In particular, the linear energy-momentum relation at low energies as well as the absence of a band gap permits the absorption in the optical and infrared regime.

Photodetectors and graphene-based solar cells require the generation of a directed photocurrent [8–12]. As proposed in [13], a directed charge current can be generated when photons are absorbed in the vicinity of a graphene edge which is subject to a perpendicular magnetic field [14]. This effect was experimentally confirmed by measuring the magneto-optical response of a suspended graphene layer [15]. Surprisingly, it was found that the induced edge current adopts much larger values than naively expected from the photon-absorption probability. More specifically, a seven-fold larger current was observed than naively expected from the absorption probability of graphene monolayers, which is about 2.3% [16–18]. This strong enhancement was dedicated to secondary electron-hole generation via Auger scattering processes [19–22]. With this reasoning, the giant magneto-photoelectric current can be understood within a two-step process. First, photons are absorbed into the dispersive edge modes and generate electron-hole pairs with energies in the eV regime. The magnetic field bends the electrons and holes in antipodal directions, which induces a directed current. Subsequently, impact ionization at the graphene edge generates further charge carriers which then also contribute to the overall current.

The response of graphene to an external electromagnetic field can be characterized by means of the optical conductivity. So far, a large number of experimental and theoretical studies have been devoted to the study of the optical response of monolayer or multilayer graphene sheets [4,23–28]. However, most of the research has focused on translationally invariant settings. As our work is related to the generation of a directed charge current which requires the breaking of charge, parity, and time-reversal symmetry, we are interested in the

spatial dependence of the photo absorption of graphene edges exposed to a perpendicular magnetic field. It is well known that the longitudinal conductivity of graphene has pronounced peaks for frequencies which are in resonance with transitions between flat bulk Landau levels [23,24]. These peaks are related to nondispersive bulk excitations and do not contribute to the directed current. Here we will focus on the absorption into the dispersive edge modes by applying the Kubo formalism.

In addition, we extend our considerations to include secondary effects, namely, electron-hole pair creation due to Auger scattering at the graphene edges. It is well known that carrier multiplication within the bulk is suppressed as the phase space for collinear scattering vanishes [22,29–31]. However, the breaking of translational invariance at the graphene edge opens up a finite volume of phase space in which carrier multiplication can take place. For low-energy excitations near the Dirac points, it is possible to describe the electronic excitations by means of an effective spinor field [3]. Employing their analytical properties, we shall discuss various selection rules for the Auger scattering rates, which are calculated via time-dependent perturbation theory.

The bare photoeffect in graphene can already be understood in the framework of noninteracting Dirac electrons in two dimensions [16,17]. Therefore, we briefly recapitulate the effective Dirac equations of single-layer graphene in Sec. II. The details of primary electron-hole generation at graphene edges will be discussed in Sec. III for two different geometries, namely, a graphene fold and a zigzag edge. The subsequent charge carrier multiplication due to impact ionization is then analyzed in Sec. IV. We give estimates for the charge carrier multiplication rates and discuss various selection rules for the decay channels.

II. DIRAC SPINORS

The carbon atoms of graphene are arranged in a hexagonal structure which can be seen as a triangular lattice with two sites in a unit cell. The electronic wave function is localized on two sublattices, which we denote with A and B . In a

tight-binding model, the stationary Schrödinger equation can be written as [32]

$$-\gamma_0 \sum_l \psi_B(\mathbf{r}_A - \tau_l) = E \psi_A(\mathbf{r}_A), \quad (1)$$

$$-\gamma_0 \sum_l \psi_A(\mathbf{r}_B + \tau_l) = E \psi_B(\mathbf{r}_B), \quad (2)$$

where γ_0 is the transfer integral between neighboring carbon atoms and the primitive translation vectors are given by $\tau_1 = a_0(0, 1/\sqrt{3})$, $\tau_2 = a_0[-1/2, -1/(2\sqrt{3})]$, and $\tau_3 = a_0(1/2, -1/2\sqrt{3})$, with $a_0 \approx 2.46 \text{ \AA}$ the lattice constant. The coordinate system was chosen such that the graphene sheet being cut parallel to the x axis has a zigzag edge. The energy dispersion vanishes linearly around the so-called Dirac points $\mathbf{K} = \frac{2\pi}{a_0}(1/3, 1/\sqrt{3})$ and $\mathbf{K}' = \frac{2\pi}{a_0}(-1/3, 1/\sqrt{3})$. Since we want to describe excitations around the Fermi level $E = 0$, we choose the following ansatz for the electron wave function:

$$\Psi_A(\mathbf{r}_A) = e^{i\mathbf{K}\cdot\mathbf{r}_A} \psi^K(\mathbf{r}_A) + e^{i\mathbf{K}'\cdot\mathbf{r}_A} \psi^{K'}(\mathbf{r}_A), \quad (3)$$

$$\Psi_B(\mathbf{r}_A) = e^{i\frac{2\pi}{3}} e^{i\mathbf{K}\cdot\mathbf{r}_B} \psi^K(\mathbf{r}_B) + e^{i\frac{2\pi}{3}} e^{i\mathbf{K}'\cdot\mathbf{r}_B} \psi^{K'}(\mathbf{r}_B), \quad (4)$$

where the phases $e^{i\mathbf{K}\cdot\mathbf{r}_{A,B}}$ and $e^{i\mathbf{K}'\cdot\mathbf{r}_{A,B}}$ are highly oscillating and $\psi_{A,B}^K$ as well as $\psi_{A,B}^{K'}$ are slowly varying envelope functions. The envelope functions can be grouped in two-component spinors, i.e., $\Psi^K = [\psi_A^K, \psi_B^K]^T$ and $\Psi^{K'} = [\psi_A^{K'}, \psi_B^{K'}]^T$, which satisfy two-component Dirac equations [33],

$$v_F \begin{pmatrix} 0 & -\hat{p}_x + i\hat{p}_y \\ -\hat{p}_x - i\hat{p}_y & 0 \end{pmatrix} \Psi^K = E \Psi^K \quad (5)$$

and

$$v_F \begin{pmatrix} 0 & \hat{p}_x + i\hat{p}_y \\ \hat{p}_x - i\hat{p}_y & 0 \end{pmatrix} \Psi^{K'} = E \Psi^{K'}. \quad (6)$$

We stress that the spinor components refer to the graphene sublattices and not to the intrinsic spin of the electronic excitations. The Fermi velocity is related to the lattice spacing and the overlap integral via $v_F = a_0\gamma_0\sqrt{3}/2$. The Dirac equations (5) and (6) have an electron-hole symmetry; therefore, each positive-energy spinor $\Psi_E^p = [\psi_A, \psi_B]^T$ has as a counterpart a negative-energy spinor $\Psi_E^h = \sigma_z \Psi_E^p$. For an infinitely extended graphene sheet, one finds the linear energy-momentum relation $E = \pm v_F |\mathbf{p}|$.

Strictly speaking, the description of electronic excitations in terms of effective Dirac spinors is only valid for energies in the vicinity of the Dirac point. Here we shall consider electronic excitations in the eV range, which is comparable to the electron hopping rate in graphene ($\approx 2.8 \text{ eV}$). Nevertheless, we shall apply the low-energy approximation since the exact dispersion relation of graphene for an excitation energy of 0.7 eV shows only deviations of, at most, 6% from the linear dispersion [3].

Moreover, the continuum description in terms of spinor fields can be justified because the lattice constant of graphene is 2.46 \AA , which is much smaller than the typical length scales associated with the magnetic field strengths considered here. In particular, for a field strength of 5 T , the magnetic length is 11 nm and the cyclotron radius, $r_{\text{cyc}} = E/(qv_F B)$, for electronic excitations with 0.7 eV is about 120 nm . Note that

these parameters are related to the experimental realization which was presented in [15].

III. OPTICAL CONDUCTIVITY

The conductivity of bare graphene has, to leading order, the frequency-independent value $\sigma = \pi\alpha_{\text{QED}} \approx 0.023$ [16–18]. The application of an external magnetic field has, as a consequence, a strong enhancement of the optical absorption in the graphene bulk due to the peaked charge carrier densities around the Landau levels [14,23,24]. One might argue that this enhancement alone could account for the large observed current. However, the bulk modes will not contribute to the directed edge current, which motivates the investigation of the absorption into the dispersive edge modes in geometries with broken translational symmetry [34].

The optical response of graphene which is subject to an external electric field $E_j(\mathbf{r}, t) = E_j(\mathbf{r}, \Omega)e^{-i\Omega t}$, i.e., a coherent laser field, can be calculated perturbatively from the Kubo formula [35]. The conductivity tensor σ_{ij} links the external field to the induced current,

$$J_i(\mathbf{r}, \Omega) = \sum_j \int d^2r' \sigma_{ij}(\mathbf{r}, \mathbf{r}', \Omega) E_j(\mathbf{r}', \Omega), \quad (7)$$

and can be expressed as a current-current correlation function. In order to evaluate the correlation function, it is convenient to employ thermal Green functions together with a subsequent analytical continuation, $\sigma_{ij}(\mathbf{r}, \mathbf{r}', \Omega) = \sigma_{ij}^T(\mathbf{r}, \mathbf{r}', i\Omega_l) \rightarrow \Omega + i\delta$). Explicitly, the correlation function of the thermal Dirac currents, $\hat{J}_i(\mathbf{r}, \tau) = -qv_F \hat{\Psi}(\mathbf{r}, \tau) \gamma^i \hat{\Psi}(\mathbf{r}, \tau)$, has the form

$$\sigma_{ij}^T(\mathbf{r}, \mathbf{r}', i\Omega_l) = -\frac{i}{\Omega} \int_0^\beta e^{i\Omega_l \tau} \langle T_\tau \hat{J}_i(\mathbf{r}, \tau) \hat{J}_j(\mathbf{r}', 0) \rangle. \quad (8)$$

The Dirac spinor $\hat{\Psi}$ contains the positive- and negative-energy modes at both Dirac points. From Eqs. (5) and (6), we find the representation of the Dirac matrices, $\gamma^0 = \text{diag}(\sigma_z, \sigma_z)$, $\gamma^1 = \text{diag}(-i\sigma_y, i\sigma_y)$, and $\gamma^2 = \text{diag}(i\sigma_x, i\sigma_x)$. Finally, the correlator (8) can be expressed in terms of thermal Green functions $G(\mathbf{r}, \mathbf{r}', \tau) = -\Theta(\tau) \langle \hat{\Psi}(\mathbf{r}, \tau) \hat{\Psi}(\mathbf{r}') \rangle$,

$$\sigma_{ij}^T(\mathbf{r}, \mathbf{r}', i\Omega_l) = \frac{i(qv_F)^2}{\Omega} \int_0^\beta e^{i\Omega_l \tau} \text{Tr} \{ \gamma^i G(\mathbf{r}, \mathbf{r}', \tau) \gamma^j \times G(\mathbf{r}', \mathbf{r}, -\tau) \}, \quad (9)$$

which then allows the evaluation in terms of Matsubara sums [36].

We assume that the wavelength of the electric field is much larger than the cyclotron radius of an electron or hole excitation and approximate $E_j(\mathbf{r}, \Omega) \approx E_j(\Omega)$. We can apply this approximation since electron-hole excitations in the eV range are generated by photons with a wavelength of about one micrometer, which are much larger than the cyclotron radius of 120 nm .

The diagonal components of the correlator then determine the conductivities for the polarizations of the electrical field perpendicular and parallel to the graphene edge,

$$\sigma_{\perp, \parallel}(\mathbf{r}, \Omega) = \text{Re} \lim_{\delta \rightarrow 0} \int d^2r' \sigma_{\perp, \parallel}^T(\mathbf{r}, \mathbf{r}', \Omega + i\delta). \quad (10)$$

The evaluation of this expression requires the explicit knowledge of the Dirac spinor, which we shall evaluate in the following for the graphene fold and the zigzag edge.

A. Graphene fold

We consider a graphene fold along the y axis with a magnetic field pointing in the z direction. The corresponding vector potential is minimally coupled to the Dirac equations (5) and (6) via $\hat{p}_y \rightarrow \hat{p}_y + qA(x)$, where q denotes the electric charge of the electron and $A(x)$ is the vector potential of the external magnetic field. The parallel momentum k is preserved due to the translation invariance along the y direction. As a consequence of the magnetic field, the excitation energies of electrons and holes can be characterized by Landau bands. Altogether, we can decompose the Dirac spinor into positive-energy (p) particle modes and negative-energy (h) hole modes in the vicinity of both Dirac points according to

$$\begin{aligned} \hat{\Psi}(\mathbf{r}, t) = & \frac{1}{2\pi\sqrt{2}} \int dk \sum_{m>0} e^{iky} \\ & \times \left[\left\{ \begin{pmatrix} \Psi_{k,m}^{p,K}(x) \\ 0 \end{pmatrix} \hat{a}_{m,k}^K + \begin{pmatrix} 0 \\ \Psi_{k,m}^{p,K'}(x) \end{pmatrix} \hat{a}_{m,k}^{K'} \right\} e^{-iE_{m,k}t} \right. \\ & \left. + \left\{ \begin{pmatrix} \Psi_{k,m}^{h,K}(x) \\ 0 \end{pmatrix} \hat{b}_{m,k}^{\dagger K} + \begin{pmatrix} 0 \\ \Psi_{k,m}^{h,K'}(x) \end{pmatrix} \hat{b}_{m,k}^{\dagger K'} \right\} e^{+iE_{m,k}t} \right], \end{aligned} \quad (11)$$

where the degeneracy of the energy bands with respect to the Dirac points was employed. From Eqs. (5) and (6), we find that the spinor components of the Dirac points are related by $\psi_{A,k,m}^{K'} = \psi_{B,k,m}^K$ and $\psi_{B,k,m}^{K'} = -\psi_{A,k,m}^K$. Furthermore, the eigenvalue equations (5) and (6) can be decoupled, which reduces the problem to the solution of the one-dimensional Schrödinger equation $v_F^2[-\partial_x^2 + V(x)]\psi_{A,k,m}^K = E_{m,k}^2 \psi_{A,k,m}^K$, with the effective potential $V(x) = [k + qA(x)]^2 + q\partial_x A(x)$.

Following the discussion in [13], a symmetric vector potential $A(-x) = A(x)$ gives rise to an additional symmetry which relates the spinor components via $\psi_{B,k,m}^K(x) = -i\mathcal{P}_{k,m}\psi_{A,k,m}^K(-x)$, where $\mathcal{P}_{k,m} = (-1)^{m+1}$ is called the pseudoparity. The lowest Landau band is labeled with $m = 1$. As a particular realization of a graphene fold with curvature radius R in a constant magnetic field, we take the vector potential to be of the form

$$A(x) = \begin{cases} B_0 R(1 - \cos \frac{x}{R}) & \text{if } |x| \leq \frac{\pi R}{2} \\ B_0 R \left(\left| \frac{x}{R} \right| - \frac{\pi}{2} + 1 \right) & \text{if } |x| > \frac{\pi R}{2}. \end{cases} \quad (12)$$

For the sake of simplicity, we choose in the following the curvature radius to be equal to the magnetic length $\ell_{B_0} = 1/\sqrt{qB_0}$. For a magnetic field of $B_0 = 5$ T, this would correspond to a curvature radius of $R = 11$ nm [37,38]. Note that graphene foldings with comparable curvature radius have been realized experimentally [39]. For a folding radius which is much smaller than the magnetic length, the setting is similar to a sharp edge such as the zigzag boundary; see below. In contrast, for a smooth bending with $R \gg \ell_{B_0}$, the charge separation is less efficient.

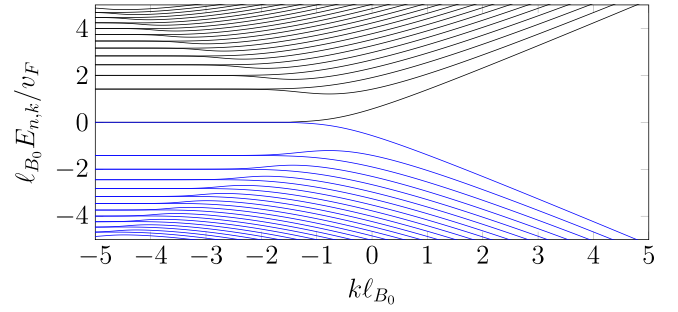


FIG. 1. Electron-hole-symmetric energy spectrum for a graphene fold in a magnetic field. The bulk modes have a flat dispersion, whereas the edge modes have $|dE/dk| \lesssim v_F$. The spectrum is degenerate with respect to the Dirac points K and K' . The energy bands have alternating pseudoparity, which is of relevance for the optical conductivity; see, also [13].

The eigensystem of the effective Schrödinger equation can be easily evaluated numerically; see Fig. 1. The electron-hole symmetry of the system is reflected in the eigenspectrum since for each electron state with positive energy $E_{m,k}$, a hole state exists with energy $E_{-m,k} = -E_{m,k}$. For large positive transversal momenta, the energy bands are dispersive with the slope given by the Fermi velocity. In a semiclassical picture, the corresponding wave functions are skipping orbits of electron and hole excitations along the graphene edge. As discussed above, the system exhibits an additional symmetry which gives rise to a pseudoparity. For large negative values of the transversal momenta k , pairs of bands with opposite pseudoparity become quasidegenerate; see Fig. 1. The corresponding states are localized inside the graphene bulk.

We shall give analytical approximations for the eigenfunctions and energy bands which are relevant for our discussion in Sec. IV A. For large and positive k , the effective potential reads $V(x) \approx k^2 + x^2 k / (\ell_{B_0}^3) + x / \ell_{B_0}^3$, and hence the eigenfunctions are boundary modes and can be expressed in terms of the harmonic-oscillator eigenfunctions,

$$\psi_{A,k,m}^K(x) \approx \phi_{m-1}[(k\ell_{B_0})^{1/4}x/\ell_{B_0}], \quad m = 1, 2, \dots \quad (13)$$

The corresponding energy bands are then

$$E_{m,k} \approx v_F \sqrt{2\sqrt{k\ell_{B_0}}(m-1/2)/\ell_{B_0}^2 + k^2}. \quad (14)$$

Asymptotically, the bands have a linear dispersion $\sim v_F k$ with an offset depending on the particular Landau band.

For large but negative k , the effective potential takes the form $V(x) \approx [k + |x|/\ell_{B_0}^2 + (1 - \pi/2)/\ell_{B_0}]^2 + \text{sign}(x)/\ell_{B_0}^2$. The corresponding eigenfunctions are dispersionless bulk modes which will not contribute to the edge current. They can be well approximated by harmonic-oscillator eigenfunctions ϕ_n . For the states of positive pseudoparity, we have

$$\psi_{A,k,1}^K(x) = \phi_0 \left(\frac{x}{\ell_{B_0}} - \ell_{B_0} k + \frac{\pi}{2} - 1 \right), \quad (15)$$

$$\begin{aligned} \psi_{A,k,2n+1}^K(x) = & \frac{1}{\sqrt{2}} \left[\phi_{n+1} \left(\frac{x}{\ell_{B_0}} - \ell_{B_0} k + \frac{\pi}{2} - 1 \right) \right. \\ & \left. - \phi_n \left(-\frac{x}{\ell_{B_0}} - \ell_{B_0} k + \frac{\pi}{2} - 1 \right) \right], \end{aligned} \quad (16)$$

with the dispersionless Landau energies $E_{2n+1} = v_F \sqrt{2n}/\ell_{B_0}$ for $n = 0, 1$, and so on. Similarly, we find, for the states of negative pseudoparity,

$$\psi_{A,k,2n}^K(x) = \frac{1}{\sqrt{2}} \left[\phi_{n+1} \left(\frac{x}{\ell_{B_0}} - \ell_{B_0} k + \frac{\pi}{2} - 1 \right) + \phi_n \left(-\frac{x}{\ell_{B_0}} - \ell_{B_0} k + \frac{\pi}{2} - 1 \right) \right], \quad (17)$$

and $E_{2n} = v_F \sqrt{2n}/\ell_{B_0}$ where $n = 1, 2$, and so on. To each Landau level with $n > 0$, we have two states with opposite pseudoparity which are quasidegenerate for sufficiently large negative k . It is noteworthy that for a superposition $\tilde{\psi}_{A,k}^K$ of two quasidegenerate states with energies E_m , one can employ the Dirac equation to construct the projection onto a state with definite pseudoparity,

$$\begin{aligned} & \frac{(-1)^{m+1} v_F}{E_{m,k}} \{ \partial_x + [k + qA(x)] \} \tilde{\psi}_{A,k}^K(-x) \\ & + \tilde{\psi}_{A,k}^K(x) \propto \psi_{A,k,m}^K(x). \end{aligned} \quad (18)$$

This turns out to be a rather useful property for the evaluation of the Auger matrix elements in Sec. IV.

As will be discussed in Sec. IV A, dispersive modes in the vicinity of the graphene edge with energies $|k\ell_{B_0}| \lesssim 1$ are of particular relevance for the charge current enhancement. In this range, the effective potential adopts the quartic form $V(x) \approx [k + x^2/(2\ell_{B_0}^2)]^2 + x/\ell_{B_0}^3$. Although the eigenfunctions cannot be given in analytical form, a reasonable approximation for the ground-state wave function can be obtained from a Gaussian variational ansatz. We find

$$\psi_{A,k,1}^K(x) = \left(\frac{a}{\pi} \right)^{1/4} \exp \left\{ -\frac{a}{2\ell_{B_0}} (x - x_0)^2 \right\}, \quad (19)$$

with $a = 1.09$ and $x_0 = -0.58\ell_{B_0} + 0.47k/\ell_{B_0}^2$. The corresponding Landau band is dispersive and can be approximated by $E_{1,k} \approx v_F(0.62/\ell_{B_0} + 0.65k)$; cf. Fig. 1. Although the energy of these modes is somewhat smaller than $v_F k$, these modes are of particular relevance for the dominating decay channels of the inelastic Auger processes.

In terms of the eigenfunctions, one can evaluate the Green functions and subsequently the optical conductivities (10). Employing the electron-hole symmetry and the pseudoparity, we obtain, at zero temperature, for each spin degree of freedom,

$$\begin{aligned} \sigma_{\perp,\parallel}(x, \Omega) &= \frac{(qv_F)^2}{4\Omega} \int dk \sum_{m,l=1}^{\infty} \delta(\Omega - E_{m,k} - E_{l,k}) \\ &\times [1 + \lambda_{\perp,\parallel}(-1)^{l+m}] \int dx' \psi_{A,k,m}^K(-x') \\ &\times \psi_{A,k,l}^K(x') \psi_{A,k,m}^K(-x) \psi_{A,k,l}^K(x) + (K \rightarrow K'). \end{aligned} \quad (20)$$

Here we have $\lambda_{\perp} = 1$ ($\lambda_{\parallel} = -1$) for the conductance perpendicular (parallel) to the fold. We infer from (20) that the conductivity perpendicular to the fold involves only transitions between states of equal pseudoparity and the states with opposite pseudoparity define the conductivity parallel to the

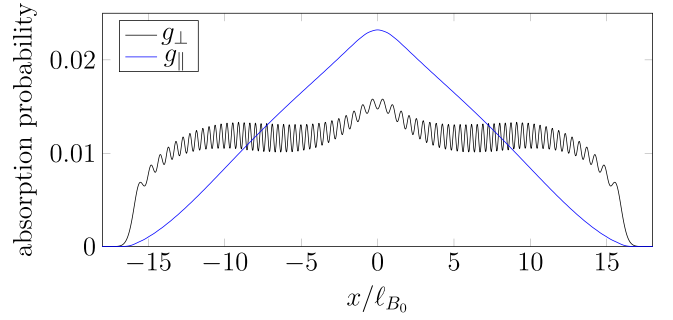


FIG. 2. Absorption probability into the boundary modes for photons with polarization perpendicular and parallel to the fold. The values do not exceed the absorption of free graphene, $g_{\text{free}} = \pi\alpha$. The absorption probability vanishes when the distance between the absorbed photon and the edge exceeds the classical cyclotron radius of the charge carriers.

edge. The absorption probability g is the ratio of absorbed energy flux, $W_{\text{abs}} = \sum_i J_i E_i$, and incident energy flux, $W_{\text{inc}} = \sum_i E_i E_i / (4\pi)$. Summing over the spin degrees of freedom gives then the relation between conductivity and absorption probability, $g_{\perp,\parallel}(x, \Omega) = 8\pi\sigma_{\perp,\parallel}(x, \Omega)$.

The polarization- and distance-dependent absorption probability into the dispersive edge channels is depicted in Fig. 2. We choose the photon energy to be $\Omega = 17v_F/\ell_{B_0}$ at a magnetic field strength of $B = 5T$, which corresponds to a photon energy of $\Omega = 1$ eV. The photon energy Ω was selected to be off resonant to the bulk Landau levels such that in the following only the absorption into the dispersive edge modes is of importance. The absorption of photons into bulk modes is not relevant for the boundary current as the generated charge carriers do not contribute to the edge current. There the longitudinal conductivity is peaked around photon energies which are resonant with the spacings of the bulk Landau levels. The height of the peaks is then only limited by the finite scattering length in graphene; see, also [23,24]. From semiclassics, we would expect that a generated electron-hole pair propagates on circular trajectories with radius $r_{\text{cyc}} = (\Omega/2)\ell_{B_0}^2/v_F = 8.5\ell_{B_0}$. Keeping this in mind, we can interpret the qualitative behavior of the g_{\perp} and g_{\parallel} . For a photon which is polarized perpendicular to the fold, the transition matrix elements are proportional to the momentum component k_{\parallel} , i.e., $\bar{\Psi}_E \gamma^1 \Psi_{-E} \propto k_{\parallel} / \sqrt{k_{\parallel}^2 + k_{\perp}^2}$. Thus, as shown in the left panel of Fig. 3, the charge carriers tend to propagate parallel to the fold before the magnetic field forces them on circular trajectories. As a consequence, many of the trajectories will intersect with the graphene fold if the electron-hole pair is generated at a distance $x \lesssim 2r_{\text{cyc}}$. This explains the rather sudden increase of $g_{\perp}(x)$ in Fig. 2. In contrast, an absorbed photon that is polarized parallel to the fold is likely to generate electron-hole pairs propagating perpendicular to the fold before their trajectories are bent by the magnetic field, $\bar{\Psi}_E \gamma^2 \Psi_{-E} \propto k_{\perp} / \sqrt{k_{\parallel}^2 + k_{\perp}^2}$. From the right panel in Fig. 3, we infer that it is rather unlikely that charge carriers are reflected from the fold if they are generated at a distance $x \lesssim 2r_{\text{cyc}}$. This, in turn, explains the gradual increase of $g_{\parallel}(x)$ towards the fold in Fig. 2.

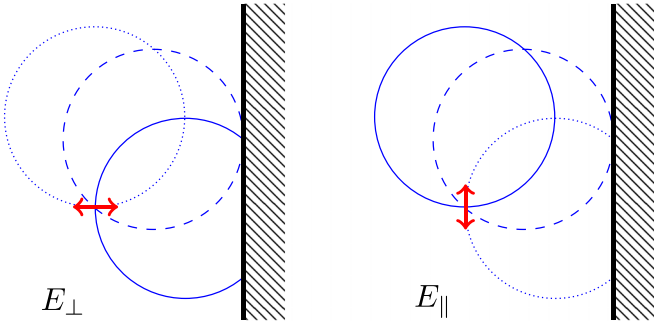


FIG. 3. Left side: Perpendicular polarized photons generate electron-hole pairs which are propagating on circular trajectories. Most likely is the propagation on the solid circle, whereas the trajectories of the dashed and dotted circles are less probable. We conclude that for this polarization, most of the generated electron-hole pairs will be reflected at the graphene edge for distances $\lesssim 2r_{\text{cyc}}$; cf. g_{\perp} in Fig. 2. Right side: The same argument shows that for parallel polarized photons which are absorbed at a distance $\sim 2r_{\text{cyc}}$ from the edge, the reflection of the generated charge carriers at the edge is unlikely. A significant absorption can only be expected when the photon is absorbed at a distance $\sim r_{\text{cyc}}$ to the edge, which explains the gradual increase of g_{\parallel} in Fig. 2.

The spatial oscillations of g_{\perp} occur independently of the respective realization of the graphene edge and are discussed in Sec. III C.

B. Zigzag boundary

As noted before, the coordinate system for the tight-binding equations (1) and (2) was selected such that a zigzag boundary is parallel to the x axis. Therefore, we take the nonvanishing component of the vector potential to be in the x direction, $A_x(y) = -B_0y$. As in the fold geometry, the two Dirac points can be treated separately. After decoupling the Dirac equations (5) and (6), one obtains the effective Schrödinger equations

$$[-\partial_y^2 + (k - qB_0y)^2 + qB_0]\psi_{A,k,m}^K = \frac{E_{m,k}^2}{v_F^2}\psi_{A,k,m}^K \quad (21)$$

$$\begin{aligned} \hat{\Psi}(\mathbf{r}, t) = & \frac{1}{2\pi\sqrt{2}} \int dk \sum_{m=0} e^{ikx} \left[\begin{pmatrix} 0 \\ \Psi_{k,m}^{p,K'}(y) \end{pmatrix} \hat{a}_{m,k}^{K'} e^{-iE_{m,k}^{K'}t} + \begin{pmatrix} 0 \\ \Psi_{k,m}^{h,K'}(y) \end{pmatrix} \hat{b}_{m,k}^{K'} e^{+iE_{m,k}^{K'}t} \right] + \frac{1}{2\pi\sqrt{2}} \int dk \sum_{m>0} e^{ikx} \\ & \times \left[\begin{pmatrix} \Psi_{k,m}^{p,K}(y) \\ 0 \end{pmatrix} \hat{a}_{m,k}^K e^{-iE_{m,k}^K t} + \begin{pmatrix} \Psi_{k,m}^{h,K}(y) \\ 0 \end{pmatrix} \hat{b}_{m,k}^K e^{+iE_{m,k}^K t} \right] + \frac{1}{2\pi} \int dk e^{ikx} \begin{pmatrix} \Psi_{k,0}^K(y) \\ 0 \end{pmatrix} \hat{a}_{0,k}^K. \end{aligned} \quad (23)$$

The components of $\Psi_{k,m}^{h,K,K'}(y)$ and $\Psi_{k,m}^{p,K,K'}(y)$ can taken to be real [cf. Eqs. (5)]. After some algebra, we obtain, for the conductance,

$$\begin{aligned} \sigma_{\perp,\parallel}(y, \Omega) = & \frac{(qv_F)^2}{4\Omega} \int dk \int dy' \sum_{l=1}^{\infty} \left\{ \sum_{m=1}^{\infty} \delta(\Omega - E_{m,k}^K - E_{l,k}^K) \psi_{A,k,l}^K(y') \psi_{B,k,m}^K(y') [\psi_{A,k,l}^K(y) \psi_{B,k,m}^K(y) + \lambda_{\perp,\parallel} \psi_{A,k,m}^K(y) \psi_{B,k,l}^K(y)] \right. \\ & \left. + \delta(\Omega - E_{l,k}^K) \psi_{A,k,l}^K(y') \psi_{B,k,0}^K(y') \psi_{A,k,l}^K(y) \psi_{B,k,0}^K(y) \right\} + \frac{(qv_F)^2}{4\Omega} \int dk \int dy' \sum_{l,m=0}^{\infty} \left\{ \delta(\Omega - E_{m,k}^{K'} - E_{l,k}^{K'}) \psi_{A,k,l}^{K'}(y') \right. \\ & \left. \times \psi_{B,k,m}^{K'}(y') [\psi_{A,k,l}^{K'}(y) \psi_{B,k,m}^{K'}(y) + \lambda_{\perp,\parallel} \psi_{A,k,m}^{K'}(y) \psi_{B,k,l}^{K'}(y)] \right\}. \end{aligned} \quad (24)$$

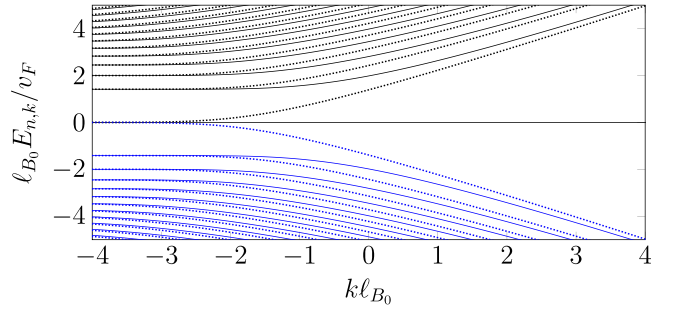


FIG. 4. Energy bands for a graphene sheet with zigzag edge in a magnetic field; see, also [42]. The dotted curves correspond to the energy bands for the modes in the vicinity of the K' point, whereas the energy bands for the second Dirac point K are represented by solid lines. The boundary condition induces a zero-energy mode at K .

and

$$[-\partial_y^2 + (k - qB_0y)^2 - qB_0]\psi_{A,k,m}^{K'} = \frac{E_{m,k}^2}{v_F^2}\psi_{A,k,m}^{K'} \quad (22)$$

We choose the graphene sheet to be terminated at the A sublattice, which implies the boundary condition $\psi_{A,k,m}^K(y=0) = \psi_{A,k,m}^{K'}(y=0) = 0$. The energy bands are shown in Fig. 4 and the corresponding eigenfunctions can be expressed in terms of parabolic cylinder functions [40,41]. As can be seen from the energy spectrum, the degeneracy of the two Dirac points is lifted due to the boundary condition. The asymptotics of the energy bands for large positive and large negative transversal momenta coincides with the spectrum of the graphene fold. However, a key difference to the graphene fold is the appearance of a localized mode at the zigzag boundary which has vanishing energy. The spinor component $\psi_{A,k,0}^K(y)$ vanishes identically, whereas the nonzero spinor component is spatially localized, $\psi_{B,k,0}^K(y) \sim \exp[-(qB_0y - k)^2/(2qB_0)]$ [14]. Decomposing the Dirac spinor into eigenmodes which are labeled by the parallel momentum, the Landau band, and the Dirac point, we obtain

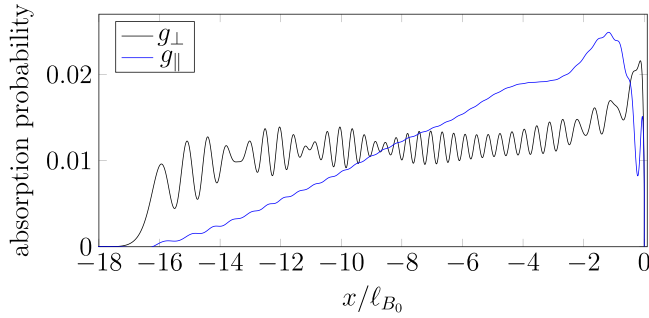


FIG. 5. Absorption probability into the dispersive edge modes for the polarizations perpendicular and parallel to the zigzag edge. The curves show the same qualitative behavior as the absorption probabilities around a graphene fold. The peaks in the vicinity of $x = 0$ are mainly due to the presence of the zero-energy mode.

As for the fold geometry [cf. (20)], the conductivity is determined by the generation of electron-hole pairs at K and K' . However, for the zigzag boundary, the excitations around the Dirac points contribute differently to the absorption probability. The presence of the zero-energy mode at the Dirac point K permits the absorption of the photon energy into a single electron or hole excitation; see Eq. (24). The qualitative behavior of the absorption probabilities g_{\perp} and g_{\parallel} can be justified as in the graphene fold.

From Figs. 2 and 5, we infer that the maximum absorption probability into the edge modes does not exceed the absorption of monolayer graphene, $g_0 = \pi\alpha_{\text{QED}}$. Altogether, we conclude that the large current observed in [15] cannot be traced back to an enhanced absorption. As a possible explanation for this effect, we shall consider estimates for charge carrier multiplication rates due to impact ionization.

C. Oscillations of the conductivity

In Figs. 2 and 5, we see that g_{\perp} shows characteristic oscillations, whereas there are only small periodic modulations of g_{\parallel} in Fig. 5. This can be understood directly from the mode decompositions (20) and (24), which schematically have the form

$$g_{\perp}(y) = \sum_K \sum_{l,m} \int dk \alpha_{l,m}^K(k) \times [\psi_{A,k,l}^K(y)\psi_{B,k,m}^K(y) + \psi_{A,k,m}^K(y)\psi_{B,k,l}^K(y)] \quad (25)$$

and

$$g_{\parallel}(y) = \sum_K \sum_{l,m} \int dk \beta_{l,m}^K(k) \times [\psi_{A,k,l}^K(y)\psi_{B,k,m}^K(y) - \psi_{A,k,m}^K(y)\psi_{B,k,l}^K(y)]. \quad (26)$$

The coefficients $\alpha_{l,m}^K(k)$ and $\beta_{l,m}^K(k)$ contain overlap integrals which become rather small unless $l \sim m$. From this and the energy conservation, $E_{m,k}^K + E_{l,k}^K = \Omega$, we conclude that the dominant contributions originate from electron and hole excitations with energies $E_{m,k}^K \approx \Omega/2$. Evaluating the wave

functions within Wigner-Kramers-Brillouin (WKB) approximation, we find that

$$\psi_{A,k,l}^K(y)\psi_{B,k,m}^K(y) + \psi_{A,k,m}^K(y)\psi_{B,k,l}^K(y) \sim \sin\left(2 \int_0^y dy' \sqrt{\frac{\Omega^2}{(2v_F)^2} - V_k(y')}\right), \quad (27)$$

where $V_k(y)$ is the effective potential which was explicitly given for the graphene fold below relation (11). For the zigzag boundary, the effective potentials for both Dirac points can be read off from the eigenvalue equations (21) and (22). We deduce that oscillations of g_{\perp} have a periodicity $\sim v_F/\Omega$ with small spatial variations due to the effective potentials. The total perpendicular absorption g_{\perp} contains a sum of functions which are of the form (27) with different values of k . Since the potentials $V_k(y)$ vary with transversal momentum k , the sum involves a superposition of oscillations with different periodicity. This explains the beating effect, which is rather apparent in Fig. 5.

In contrast, employing the WKB approximation for the mode decomposition of g_{\parallel} leads to

$$\psi_{A,k,l}^K(y)\psi_{B,k,m}^K(y) - \psi_{A,k,m}^K(y)\psi_{B,k,l}^K(y) \sim \sin\left(\frac{\Omega}{2} \int_0^y dy' \frac{E_{l,k}^K - E_{m,k}^K}{\sqrt{\frac{\Omega^2}{(2v_F)^2} - V_k(y')}}\right). \quad (28)$$

These spatial oscillations have much larger periodicities, $\sim v_F/(E_{l,k}^K - E_{m,k}^K)$, which explains the rather smooth increase of g_{\parallel} towards the graphene edge. The tiny oscillations of g_{\parallel} in Fig. 5 originate from higher-order WKB corrections.

IV. SECONDARY ELECTRON-HOLE PAIR CREATION

Auger processes have been thoroughly studied for translationally invariant graphene sheets [43–46]. There the energy-momentum conservation together with the linear dispersion relation restricts the phase space for interactions to one dimension, i.e., only collinear processes are allowed [43]. In contrast, a graphene edge breaks the translational invariance and opens up a finite phase-space volume for carrier multiplication.

Our analysis will reside on the bare Coulomb Hamiltonian,

$$\hat{H}_{\text{Coulomb}} = \frac{q^2}{2} \int d^2r \int d^2r' \frac{\hat{\rho}(\mathbf{r})\hat{\rho}(\mathbf{r}')}{4\pi\epsilon_0|\mathbf{r}-\mathbf{r}'|}, \quad (29)$$

where the electron densities can be written in terms of the Dirac fields as

$$\hat{\rho}(\mathbf{r}) = \sum_{\sigma} \{[\hat{\Psi}_{\sigma}^K(\mathbf{r})]^{\dagger} \hat{\Psi}_{\sigma}^K(\mathbf{r}) + [\hat{\Psi}_{\sigma}^{K'}(\mathbf{r})]^{\dagger} \hat{\Psi}_{\sigma}^{K'}(\mathbf{r})\}. \quad (30)$$

Here we employed the expressions (3) and (4) and neglected rapidly oscillating interference terms of the two Dirac points, $\sim e^{i(\mathbf{K}-\mathbf{K}')\cdot\mathbf{r}}$. The label σ denotes the spin degree of freedom which was suppressed in the previous sections.

We emphasize that our study is solely based on Fermi's golden rule and our analysis for carrier multiplication around the graphene edge shall give only a rough order-of-magnitude

estimate for the charge carrier multiplication rates. The effective fine-structure constant in graphene, α_{graphene} , is much larger than α_{QED} due to a relative factor $c/v_F \approx 300$. This can be understood intuitively from the fact that the Fermi velocity is much slower than the speed of light and thus the charge carriers have more time to interact. Although the effective fine-structure constant will be diminished somewhat due to electronic screening, we shall neglect this in our approach since this effect is rather weak at the Dirac points [47,48]. If the graphene layer is immersed in a dielectric-media effective dielectric constant $\bar{\epsilon}$, the effective fine-structure constant of the Coulomb interaction will change according to $\alpha_{\text{graphene}} \rightarrow \alpha_{\text{graphene}}/\bar{\epsilon}$ [49,50]. This reduces the effective expansion parameter and improves the accuracy of our first-order approach. As a consequence, the calculated scattering rates for the Auger processes would be diminished by a factor $1/\bar{\epsilon}^2$.

Another aspect of secondary effects in graphene is the coupling of electrons and holes to phononic excitations [51–53]. However, as the dimensionless electron-phonon coupling is at least an order of magnitude smaller than the direct electron-electron interaction (see, for example, [51]), we shall neglect it in the following. Nevertheless, we would like to note that the electron-phonon coupling can be enhanced if the phonons are brought into resonance with inter-Landau-level transitions [54,55].

We consider Auger-type inelastic scattering of an incoming electron, $|\text{in}\rangle = |k_{\text{in}}, n_{\text{in}}\rangle$, to an outgoing electron, $|\text{out}\rangle = |k_{\text{out}}, n_{\text{out}}\rangle$, while creating an electron-hole pair $|\text{el, hole}\rangle = |k_{\text{el}}, n_{\text{el}}, k_{\text{hole}}, n_{\text{hole}}\rangle$. Using standard first-order perturbation theory, we find, for the transition matrix elements,

$$M(\text{in} \rightarrow \text{out}, \text{el}, \text{hole}) = -i \int dt \langle \text{out}, \text{el}, \text{hole} | \hat{H}_{\text{Coulomb}} | \text{in} \rangle. \quad (31)$$

Summing the absolute square of (31) over all final states gives the leading-order result for the impact ionization rate. If we assume that the momentum of the incoming electron is in the vicinity of the Dirac point K and the secondary electron-hole pair is generated around K' , the probability per unit time reads

$$\frac{\mathcal{P}^{K, \sigma \rightarrow K', \lambda}}{T} = \frac{v_F \alpha_{\text{graphene}}^2}{8\pi} \int dk_{\text{out}} \mathcal{H}^{K, \sigma \rightarrow K', \lambda}(k_{\text{out}}). \quad (32)$$

The integrand

$$\mathcal{H}^{K, \sigma \rightarrow K', \lambda}(k_{\text{out}}) = \frac{v_F}{\left| \frac{d\mathcal{F}}{dk_{\text{el}}} \right|} |\mathcal{I}^{K, \sigma \rightarrow K', \lambda}|^2 |_{\mathcal{F}=0} \quad (33)$$

is determined by an overlap integral specifying the Coulomb interaction between the charge densities,

$$\begin{aligned} \mathcal{I}^{K, \sigma \rightarrow K', \lambda} &= \int dx \int dx' [\Psi_{k_{\text{el}}, n_{\text{el}}}^{\text{p}, K'}(x)]^\dagger \Psi_{k_{\text{hole}}, n_{\text{hole}}}^{\text{h}, K'}(x) \\ &\times K_0(|k_{\text{in}} - k_{\text{out}}| D(x, x')) [\Psi_{k_{\text{out}}, n_{\text{out}}}^{\text{p}, K}(x')]^\dagger \\ &\times \Psi_{k_{\text{in}}, n_{\text{in}}}^{\text{p}, K}(x'), \end{aligned} \quad (34)$$

and the weight factor $d\mathcal{F}/dk_{\text{el}}$; see below. The Coulomb interaction is encoded in the Bessel function K_0 , which arises after the integration over the momentum component parallel to the edge. Its argument contains the momentum difference between the incoming and outgoing electron and the

function $D(x, x')$ that measures the distance of the charge densities perpendicular to the fold. Two variables can be eliminated using the momentum conservation, $k_{\text{in}} - k_{\text{out}} = k_{\text{el}} - k_{\text{hole}}$, and the energy conservation, $\mathcal{F} = E_{n_{\text{in}}, k_{\text{in}}} - E_{n_{\text{out}}, k_{\text{out}}} - E_{n_{\text{el}}, k_{\text{el}}} - E_{n_{\text{hole}}, k_{\text{hole}}} \equiv 0$. The weight factor $d\mathcal{F}/dk_{\text{el}}$ in (33) ensures the local reparametrization invariance of the integral. The reparametrization invariance for the whole integration domain does not exist, in general, since $dk_{\text{out}}/dk_{\text{el}}$ can become singular. Nevertheless, it is always possible to find a parametrization for \mathcal{H} which governs the complete integration domain.

The matrix elements for impact ionization in the same Dirac valley but opposite spin are analogous to (32). In contrast, when the spin and the valley index are the same, the outgoing electron is indistinguishable from the generated electron. Therefore, the probability $\mathcal{P}^{K, \sigma \rightarrow K, \sigma}$ is now determined by overlap integrals which satisfy an exchange symmetry,

$$\begin{aligned} \mathcal{I}^{K, \sigma \rightarrow K, \sigma} &= \int dx \int dx' [\Psi_{k_{\text{el}}, n_{\text{el}}}^{\text{p}, K}(x)]^\dagger \Psi_{k_{\text{hole}}, n_{\text{hole}}}^{\text{h}, K}(x) \\ &\times K_0(|k_{\text{in}} - k_{\text{out}}| D(x, x')) [\Psi_{k_{\text{out}}, n_{\text{out}}}^{\text{p}, K}(x')]^\dagger \\ &\times \Psi_{k_{\text{in}}, n_{\text{in}}}^{\text{p}, K}(x') - (k_{\text{out}}, n_{\text{out}} \leftrightarrow k_{\text{el}}, n_{\text{el}}). \end{aligned} \quad (35)$$

Before we discuss the specific settings of a graphene fold and a zigzag boundary, two remarks are in order. First, the leading-order perturbation theory may not be very accurate since the dimensionless expansion parameter is larger than unity, $\alpha_{\text{graphene}} = \alpha_{\text{QED}} c/v_F \approx 2.2$. Second, we will not consider Auger recombination and assume that the generated charge carriers reach the bond contacts of the graphene boundary before electron-hole annihilation occurs. Electron-hole annihilation can, in principle, be considered within a Boltzmann-equation approach [43]. However, we expect the recombination rates to be negligible for sufficiently small electron-hole densities; see, also [56].

A. Graphene fold

A graphene fold breaks translation invariance without terminating the graphene sheet. As in Sec. III A, we assume the magnetic length ℓ_B and the fold radius R to be equal. The spatial separation $D(x, x')$ of the charge carrier densities can be deduced by simple geometric considerations from Fig. 6.

An exact selection rule occurs due to the pseudoparity, which was briefly discussed in Sec. III A. As a consequence, the integrals $\mathcal{I}^{K, \sigma \rightarrow K, \lambda}$ and $\mathcal{I}^{K, \sigma \rightarrow K', \lambda}$ vanish identically unless the sum of the Landau-level indices, $n_{\text{in}} + n_{\text{out}} + n_{\text{el}} + n_{\text{hole}}$, equals an odd integer. From the allowed transitions, only a few decay channels dominate the process, whereas most of the channels will be suppressed by several orders of magnitude. If the number of nodes of the wave functions $\Psi_{k_{\text{in}}, n_{\text{in}}}^{\text{p}, K}$ and $\Psi_{k_{\text{out}}, n_{\text{out}}}^{\text{p}, K}$ are very different from each other, the wave functions are nearly orthogonal, which renders the overlap integral (34) exponentially small. The same is true for $\Psi_{k_{\text{el}}, n_{\text{el}}}^{\text{p}, K'}$ and $\Psi_{k_{\text{hole}}, n_{\text{hole}}}^{\text{p}, K'}$. Therefore, the decay channels between the Dirac points K and K' can usually be neglected unless $n_{\text{el}} \sim n_{\text{hole}}$ and $n_{\text{in}} \sim n_{\text{out}}$.

Furthermore, a strong oscillation of the integrands will render the overlap integrals exponentially small. In order to keep

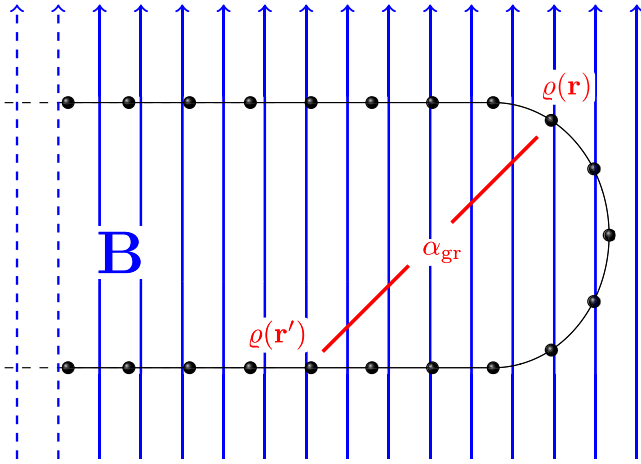


FIG. 6. Sketch of the graphene fold in an external magnetic field. Secondary electron-hole pairs are generated via the Coulomb interaction.

the total number of nodes of the integrand in Eq. (34) as small as possible, we can conclude that for an incoming electron at Landau level n_{in} , the following approximate selection rule applies:

$$n_{\text{out}} \in \{n_{\text{in}}, n_{\text{in}} \pm 1\} \quad \text{and} \quad n_{\text{el}} \sim n_{\text{hole}} \sim 1. \quad (36)$$

For transitions within the same Dirac point, we also obtain relevant contributions for $n_{\text{out}} \sim n_{\text{hole}} \gg n_{\text{in}} \sim n_{\text{el}}$, a direct consequence of the exchange symmetry; see Eq. (35).

We illustrate our findings and consider the decay process of an incoming electron with $n_{\text{in}} = 5$ and $k_{\text{in}} = 10/\ell_{B_0}$. For a magnetic field of $B_0 = 5T$, this would correspond to an initial energy of $E_{n_{\text{in}}, k_{\text{in}}} = 0.7$ eV. For transitions involving states of both Dirac points, we list the rates for various decay channels in Table I. Although the applicability of first-order perturbation theory should be doubted and not every generated charge carrier will contribute to the overall current (see below), we see from Table I that each of the largest decay channels generates between 80 and 90 electron-hole pairs within one picosecond, which is about 10 electron-hole pairs within the distance of a classical cyclotron radius.

Figure 7 shows the magnitude of the integrals which determine the decay channels, $\mathcal{P}^{K, \sigma \rightarrow K', \lambda}(n_{\text{in}} \rightarrow n_{\text{out}}, n_{\text{el}}, n_{\text{hole}})$. Transitions which do not fulfill the relation (36) are strongly suppressed.

For transitions in the vicinity of one Dirac point, we list the dominating integrals in Table II. Here, all rates come in pairs, which is a direct consequence of the exchange sym-

TABLE I. The first two rows specify the largest decay rates for transitions $K \rightarrow K'$ for an incoming electron with $n_{\text{in}} = 5$ and $k_{\text{in}} = 10/\ell_{B_0}$. The decay rates in the third and fourth lines are at least one magnitude smaller since they do not fulfill (36).

n_{out}	n_{el}	n_{hole}	\mathcal{P}/T (s^{-1})
4	1	1	9.4×10^{13}
6	1	1	8.1×10^{13}
1	4	1	1.5×10^{12}
1	6	1	4.5×10^{11}

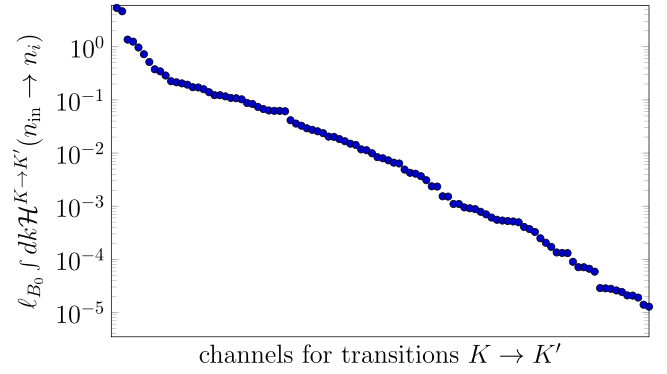


FIG. 7. Overlap integrals which determine the decay probabilities per unit time. Here we only consider the channels for which the incoming electron is in the vicinity of the K point and the outgoing electron-hole pair is generated around the K' point. The corresponding rates for the two largest integrals are listed in Table I. As can be seen here, the remaining channels are strongly suppressed.

metry of (35), from which follows that $\mathcal{P}^{K, \sigma \rightarrow K, \sigma}(n_{\text{out}}, n_{\text{el}}) = \mathcal{P}^{K, \sigma \rightarrow K, \sigma}(n_{\text{el}}, n_{\text{out}})$. Comparing the corresponding rates of Tables I and II, we find $\mathcal{P}^{K, \sigma \rightarrow K, \sigma} \lesssim \mathcal{P}^{K, \sigma \rightarrow K', \sigma}$. This small suppression in comparison to the $K \rightarrow K'$ rates originates from destructive interference, which is rather small unless $n_{\text{out}} \sim n_{\text{el}}$; cf. Eqs. (36) and (35). In Fig. 8, we show the matrix elements determining the $K \rightarrow K$ transitions, sorted by size.

Summing over the spin configurations, both Dirac points, and all final configurations for the outgoing electron and the generated electron-hole pair, we find for our example the total impact ionization rate,

$$\begin{aligned} \frac{\mathcal{P}_{\text{total}}}{T} &= \frac{1}{T} \sum_{\lambda} \sum_{n_i} (3\mathcal{P}_{n_i}^{K, \sigma \rightarrow K', \lambda} + \mathcal{P}_{n_i}^{K, \sigma \rightarrow K, \lambda}) \\ &\approx 1.4 \times 10^{15} \text{ s}^{-1}, \end{aligned} \quad (37)$$

which corresponds to about 180 generated electron-hole pairs within a distance of one cyclotron radius. Although some of the secondary electrons and holes are generated in the bulk and do not contribute to the total current (see below), our estimate shows the efficiency of the charge carrier multiplication.

One of the dominating channels in the pair production process with transitions $K \rightarrow K$ is specified by the quantum numbers $n_{\text{in}} = 5$, $n_{\text{out}} = 1$, $n_{\text{el}} = 4$, and $n_{\text{hole}} = 1$. The corresponding integrand $\mathcal{H}^{K, \sigma \rightarrow K, \sigma}$ for this decay channel is shown in the upper panel of Fig. 9. In the lower panel of Fig. 9, we see the currents $J = dE/dk$ for the outgoing electron and the generated electron-hole pair. For $k_{\text{out}} \lesssim -1.5/\ell_{B_0}$, the whole

TABLE II. Decay rates of the dominating channels for an incoming electron with $n_{\text{in}} = 5$ and $k_{\text{in}} = 10/\ell_{B_0}$. The rates are symmetric with respect to the interchange of n_{out} and n_{el} .

n_{out}	n_{el}	n_{hole}	\mathcal{P}/T (s^{-1})
4	1	1	8.3×10^{13}
1	4	1	8.3×10^{13}
6	1	1	7.5×10^{13}
1	6	1	7.5×10^{13}

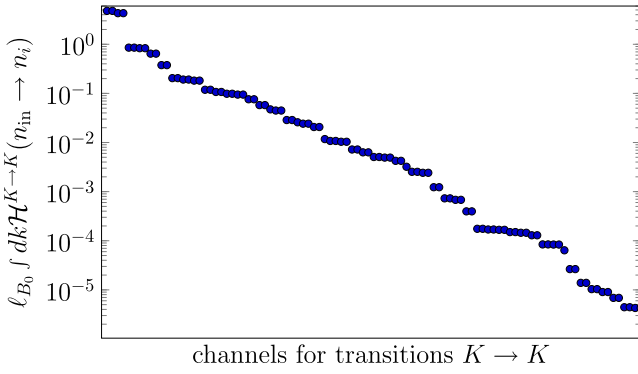


FIG. 8. Overlap integrals determining the decay probabilities per unit time in the vicinity of one Dirac point time, sorted by size, on a logarithmic scale. As a consequence of the exchange symmetry, all matrix elements occur in pairs.

energy of the incoming electron is transferred to the generated electron, whereas the generated hole and the outgoing electron are bulk modes with zero energy. In contrast, for $k_{\text{out}} \gtrsim -1.5/l_{B_0}$, the outgoing electron and the generated hole are located in the vicinity of the boundary and additional current is generated.

In our example, the function $\mathcal{H}^{K,\sigma \rightarrow K,\sigma}$ has its maximum around $k_{\text{out}} \ell_{B_0} \sim -1$. In general, the position of this maximum determines the contribution of the generated charge carriers to the overall current. To clarify this statement, we consider a transition with $n_{\text{el}} = n_{\text{in}} - 1$ and $\ell_{B_0} k_{\text{in}} \gg 1$ and $n_{\text{out}} = n_{\text{hole}} = 1$. The Coulomb integral (34) is exponentially suppressed unless $\ell_{B_0}(k_{\text{in}} - k_{\text{el}}) \ll 1$. Together with (14) and the energy conservation, we infer that the energies of the

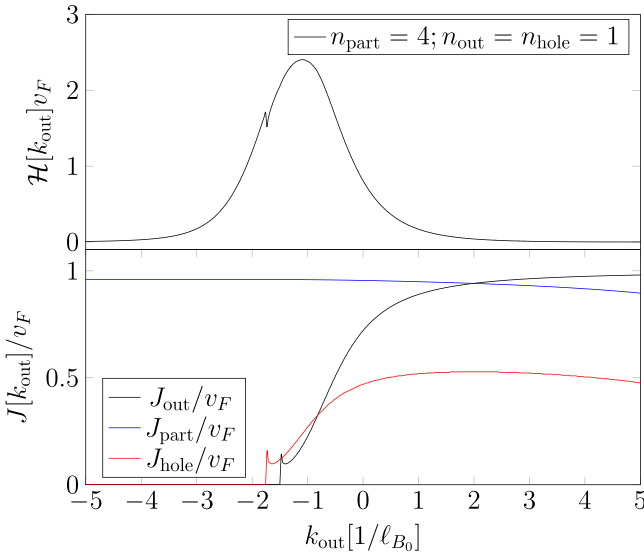


FIG. 9. Upper panel: Value of $\mathcal{H}^{K,\sigma \rightarrow K,\sigma}$ as a function of k_{out} . Lower panel: Currents related to the outgoing electron and the generated electron-hole pair. The cusps in the plots around $k_{\text{out}} = -1.5/l_{B_0}$ originate from the slope of the lowest-energy band in our model; cf. Fig. 1.

outgoing electron and the generated hole are small,

$$(E_{n_{\text{out}},k_{\text{out}}} + E_{n_{\text{hole}},k_{\text{hole}}}) = \frac{v_F}{\ell_{B_0}} \mathcal{O}\{\ell_{B_0}(k_{\text{in}} - k_{\text{el}}), 1/\sqrt{\ell_{B_0}k_{\text{in}}}\}. \quad (38)$$

Thus, the outgoing electron and the generated hole will be either zero-energy modes of the form (15) or low-energy modes at the boundary; see Eq. (19).

If $n_{\text{in}} \sim 1$ and $\ell_{B_0}k_{\text{in}} \gg 1$, we know from (13) that $\Psi_{k_{\text{in}},n_{\text{in}}}^{p,K}$ and $\Psi_{k_{\text{el}},n_{\text{el}}}^{p,K}$ are located around the edge and therefore $\mathcal{H}^{K,\sigma \rightarrow K,\sigma}$ will adopt its maximum value at $|k_{\text{out}}|\ell_{B_0} \lesssim 1$ if the wave functions $\Psi_{k_{\text{out}},n_{\text{out}}}^{p,K}$ and $\Psi_{k_{\text{hole}},n_{\text{hole}}}^{h,K}$ are both dispersive edge modes of the form (19). In contrast, for $n_{\text{in}} \gg 1$, the greatest weight of the wave functions, $\Psi_{k_{\text{in}},n_{\text{in}}}^{p,K}$ and $\Psi_{k_{\text{el}},n_{\text{el}}}^{p,K}$, are close to the classical turning points inside the bulk,

$$\frac{|x_{\text{turn}}|}{\ell_{B_0}} \approx \frac{\sqrt{2n_{\text{in}}}}{(\ell_{B_0}k_{\text{in}})^{1/4}}. \quad (39)$$

Here, $\mathcal{H}^{K,\sigma \rightarrow K,\sigma}$ adopts its maximum value if the outgoing electron and the generated hole are bulk modes. The position of the maximum of $\mathcal{H}^{K,\sigma \rightarrow K,\sigma}$ can be estimated from (15) and (39) to be at $\ell_{B_0}k_{\text{out}} \approx -\sqrt{2n_{\text{in}}}/(\ell_{B_0}k_{\text{in}})^{1/4}$.

As the bulk modes do not contribute to the total current, we conclude that initial states with small n_{in} are beneficial for the current enhancement. For these dispersive edge modes, we have $n_{\text{in}}/k_{\text{in}}\ell_{B_0} \ll 1$, which corresponds to charge excitations traveling nearly parallel to the fold. In contrast, for large n_{in} , only the final states which are inside the tail of $\mathcal{H}^{K \rightarrow K}$ at $|\ell_{B_0}k_{\text{out}}| \lesssim 1$ are relevant for the generated current.

In order to quantify our statement, we calculated the expectation value of the sum of all currents $J_k = dE/dk$, i.e.,

$$\begin{aligned} & \frac{\mathcal{C}^{K,\sigma \rightarrow K,\sigma}}{T} \\ &= \frac{\alpha_{\text{graphene}}^2}{8\pi} \int dk_{\text{out}} (J_{k_{\text{out}}} + J_{k_{\text{el}}} + J_{k_{\text{hole}}} - J_{k_{\text{in}}}) \mathcal{H}^{K,\sigma \rightarrow K,\sigma}. \end{aligned} \quad (40)$$

This quantity characterizes the number of charge carriers per unit time which contribute to the edge current. From Fig. 10, we conclude that although the number of generated charge carriers grows with increasing n_{in} , the generation of edge modes adopts its maximum value at small values of n_{in} . Going back to our initial example, we find, after summing over all final states, $\mathcal{C}_{\text{total}}/T \approx 7.8 \times 10^{14} \text{ s}^{-1}$. Comparing with (37), we conclude that only every fourth generated charge carrier will contribute to the edge current.

B. Zigzag boundary

The carrier multiplication process is a rather robust effect and we expect that the main characteristics of the decay process also hold for a graphene sheet with zigzag boundary.

Again we find that the overlap integrals $\mathcal{I}^{K,\sigma \rightarrow K,\lambda}$ and $\mathcal{I}^{K,\sigma \rightarrow K',\lambda}$ are strongly suppressed unless the approximate selection rule (36) applies. As for the fold geometry, the charge carrier multiplication is dominated by a few channels.

We took the same parameter choice as for the graphene fold. The dominant transitions $K \rightarrow K$ contain a zero-energy mode $\psi_{0,k}^K$, with one vanishing spinor component;

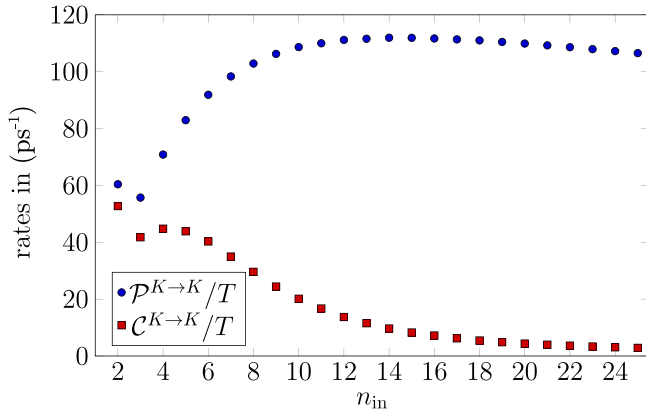


FIG. 10. We consider the decay channels from an incoming electron at Landau band n_{in} with an initial energy $E_{n_{\text{in}},k_{\text{in}}} = 0.7$ eV to the outgoing states which are specified by $n_{\text{in}} \rightarrow n_{\text{out}} = n_{\text{in}} - 1$ and $n_{\text{el}} = n_{\text{hole}} = 1$. The blue dots denote the generation rates for electron-hole pairs, whereas the red squares are the corresponding rates for additionally generated charge carriers which contribute to the edge current.

see Eq. (23). The presence of this nondispersive enlarges the phase space for these channels since momentum conservation can always be satisfied. In Fig. 11, we show the probabilities per unit time, $\mathcal{P}^{K,\sigma \rightarrow K,\sigma'}/T$, for the processes involving the zero-energy mode and $n_{\text{in}} = n_{\text{out}}$ as well as $n_{\text{hole}} = 1$. For increasing n_{in} , the weight of the corresponding wave function is moving inside the bulk, which diminishes the overlap with the electron-hole modes at the boundary. As before, this implies that small values of n_{in} are beneficial for the current enhancement.

We also found rather large rates for transitions between both graphene valleys, $K \rightarrow K'$. Matrix elements with $n_{\text{out}} = n_{\text{in}} - 1$ and $n_{\text{el}} = n_{\text{hole}} = 0$ are presented in the upper panel of Fig. 12 and are of similar magnitude as the rates in the graphene fold; cf. Fig. 10. The largest contribution to the impact ionization originates from transitions with the quantum numbers $n_{\text{in}} = n_{\text{out}} = 1$ and $n_{\text{el}} = n_{\text{hole}} = 0$; see the lower panel of Fig. 12. Note that these transitions are absent in the graphene fold due to the pseudoparity selection rule.

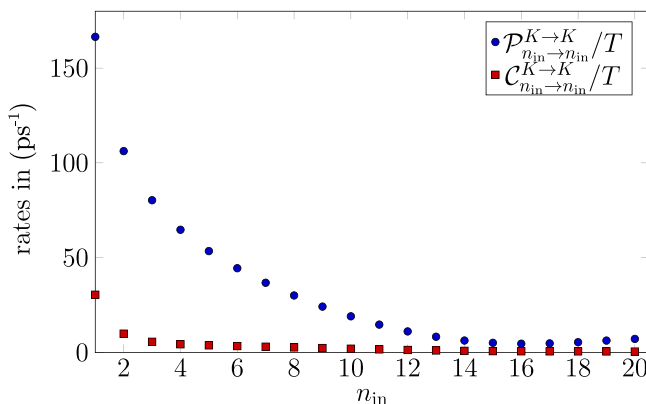


FIG. 11. Transitions within the Dirac point K are dominated by channels that contain the zero-energy mode.

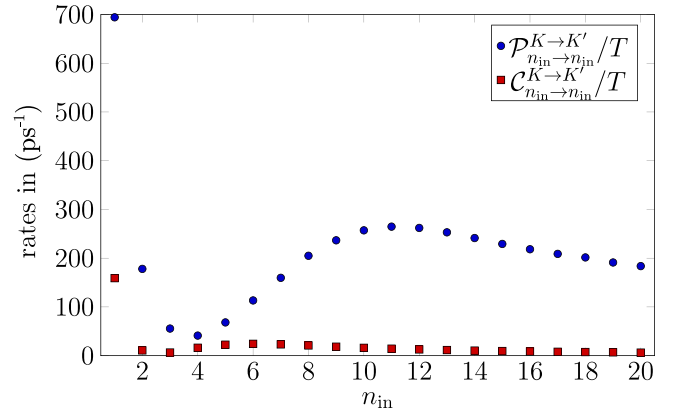
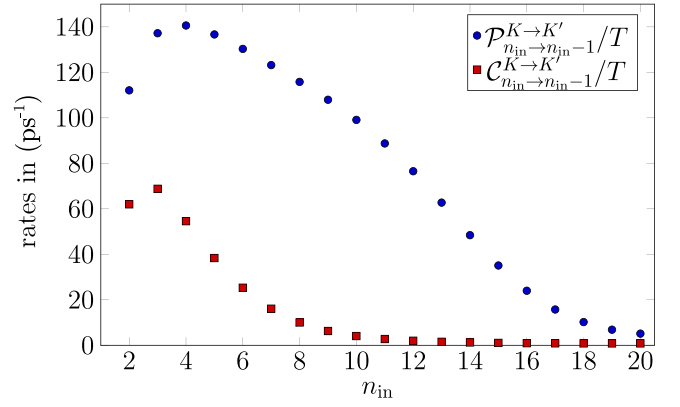


FIG. 12. Upper panel: Rates for the transitions between the two Dirac points. The quantum numbers for the incoming and outgoing electron are n_{in} and $n_{\text{out}} = n_{\text{in}} - 1$ and the electron-hole pair is generated in the state with $n_{\text{el}} = n_{\text{hole}} = 0$. The magnitude of these rates is comparable to the results we found in the graphene fold; see Fig. 10. Lower panel: Rates for channels which are specified by $n_{\text{in}} = n_{\text{out}}$ and $n_{\text{el}} = n_{\text{hole}} = 0$ are dominating the Auger process for small values of n_{in} .

V. CONCLUSIONS AND OUTLOOK

We analyzed the primary magneto-optical absorption of graphene and the subsequent electron-hole generation due to impact ionization. The bare magneto-photoelectric current, in particular the absorption into the dispersive edge modes, does not exceed the well-known value for graphene monolayers. However, subsequent impact ionization leads to charge carrier multiplication and therefore to a strong enhancement of the photocurrent. We found that charge carrier multiplication depends on the incident angle between the incoming electron and graphene edge; small impact angles are particularly advantageous for current amplification. The presence of a finite phase-space volume due to the absence of translation invariance makes this effect rather robust. However, the specific enhancement will depend on the particular boundary condition of the graphene edge. The derived exact and approximate selection rules show that only a small subset of the decay channels will significantly contribute to the dynamics. An illustration of the exact and approximate selection rules is given in Figs. 13 and 14. The use of these results could allow the efficient implementation of the relaxation dynamics using a Boltzmann equation approach. Although we expect that the

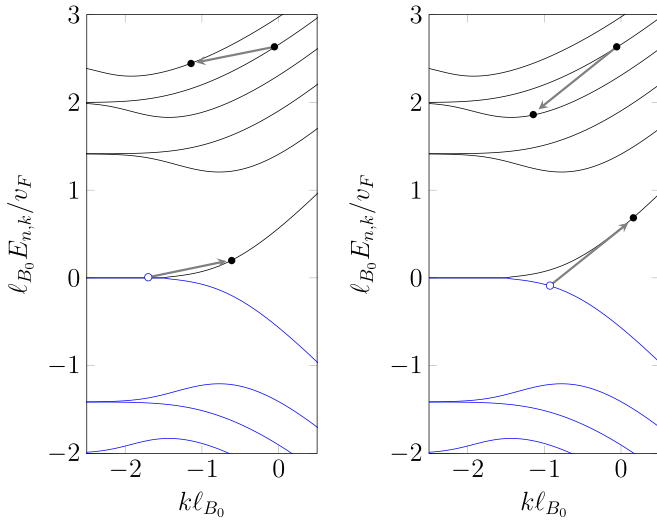


FIG. 13. Dominant decay channels in the graphene fold where the Landau band index of an electron is increased (left panel) or decreased (right panel) while creating an electron-hole pair. Since the sum of all Landau band indices of the involved charge carriers has to be odd, processes with $n_{in} = n_{out}$ and $n_{el} = n_{hole} = 1$ are forbidden.

qualitative behavior of the charge multiplication can already be captured within leading-order perturbation theory, a quantitative prediction should include higher-order corrections of the scattering processes.

For our particular example, we found that the rate of secondary electron-hole creation is of the order of 10^{14} s^{-1} . This would correspond to the generation of about 10^2 charge carriers within a distance of one micrometer. This value overestimates the findings of the experimental findings which showed a sevenfold increase of the magneto-photoelectric current [15]. However, as noted above, the leading-order perturbation theory should be taken with caution since it involves the effective fine-structure constant of graphene, which is not a small parameter. Also, possible recombination processes of electron-hole pairs have not been considered in our

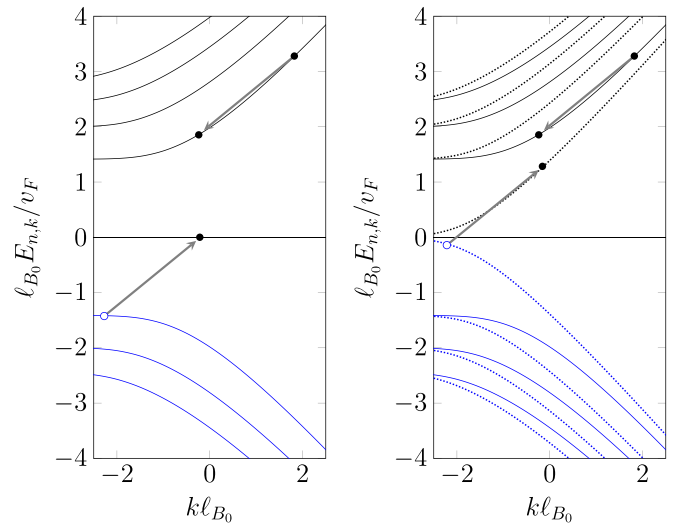


FIG. 14. Dominant decay channels at a zigzag edge. Although no exact selection rules exist, the dominating channels fulfill the condition (36). Left panel: Auger process at the K point in which the zero-energy mode ensures the momentum conservation. Right panel: Auger process where an electronic excitation near the K point generates an electron-hole pair at the K' point. Energies around the K (K') point are indicated by solid (dotted) lines.

calculations. Altogether, the experimental setup will not be captured in total within our idealized description. Nevertheless, our results are qualitatively consistent with the experiment and show that Auger processes are viable to account for the strong amplification of the magneto-photoelectric response.

ACKNOWLEDGMENTS

The authors thank S. Winnerl and C. Kohlfürst for valuable discussions. This research is funded by the German Research Foundation DFG (Grants No. 278162697 - SFB 1242 and No. 398912239).

- [1] A. A. Balandin, S. Ghosh, W. Bao, I. Calizo, D. Teweldebrhan, F. Miao, and C. N. Lau, Superior thermal conductivity of single-layer graphene, *Nano Lett.* **8**, 902 (2008).
- [2] A. S. Mayorov, R. V. Gorbachev, S. V. Morozov, L. Britnell, R. Jalil, L. A. Ponomarenko, P. Blake, K. S. Novoselov, K. Watanabe, T. Taniguchi, and A. K. Geim, Micrometer-scale ballistic transport in encapsulated graphene at room temperature, *Nano Lett.* **11**, 2396 (2011).
- [3] A. H. Castro Neto, F. Guinea, N. M. R. Peres, K. S. Novoselov, and A. K. Geim, The electronic properties of graphene, *Rev. Mod. Phys.* **81**, 109 (2009).
- [4] R. Nair, P. Blake, A. N. Grigorenko, K. S. Novoselov, T. J. Booth, T. Stauber, N. M. R. Peres, and A. K. Geim, Fine structure constant defines visual transparency of graphene, *Science* **320**, 1308 (2008).
- [5] P. Ma, Y. Salamin, B. Baeuerle, A. Josten, W. Heni, A. Emboras, and J. Leuthold, Plasmonically enhanced graphene photodetector featuring 100 Gbit/s data reception, high responsivity, and compact size, *ACS Photon.* **6**, 154 (2019).
- [6] F. Bonaccorso, Z. Sun, T. Hasan, and A. C. Ferrari, Graphene photonics and optoelectronics, *Nat. Photon.* **4**, 611 (2010).
- [7] F. H. L. Koppens, T. Mueller, Ph. Avouris, A. C. Ferrari, M. S. Vitiello, and M. Polini, Photodetectors based on graphene, other two-dimensional materials and hybrid systems, *Nat. Nanotechnol.* **9**, 780 (2014).
- [8] J. C. W. Song, M. S. Rudner, C. M. Marcus, and L. S. Levitov, Hot carrier transport and photocurrent response in graphene, *Nano Lett.* **11**, 4688 (2011).
- [9] S. Candussio, M. V. Durnev, S. A. Tarasenko, J. Yin, J. Keil, Y. Yang, S.-K. Son, A. Mishchenko, H. Plank, V. V. Bel'kov, S. Slizovskiy, V. Fal'ko, and S. D. Ganichev, Edge photocurrent driven by terahertz electric field in bilayer graphene, *Phys. Rev. B* **102**, 045406 (2020).
- [10] Q. Ma, C. H. Lui, J. C. W. Song, Y. Lin, J. F. Kong, Y. Cao, T. H. Dinh, N. L. Nair, W. Fang, K. Watanabe, T. Taniguchi, S.-Y. Xu, J. Kong, T. Palacios, N. Gedik, N. M. Gabor, and P. Jarillo-Herrero, Giant intrinsic photoresponse in pristine graphene, *Nat. Nanotechnol.* **14**, 145 (2019).

- [11] M. Shimatani, S. Ogawa, D. Fujisawa, S. Okuda, Y. Kanai, T. Ono, and K. Matsumoto, Photocurrent enhancement of graphene phototransistors using p-n junction formed by conventional photolithography process, *Jpn. J. Appl. Phys.* **55**, 110307 (2016).
- [12] D. Sun, G. Aivazian, A. M. Jones, J. S. Ross, W. Yao, D. Cobden, and X. Xu, Ultrafast hot-carrier-dominated photocurrent in graphene, *Nat. Nanotechnol.* **7**, 114 (2012).
- [13] F. Queisser and R. Schützhold, Strong Magnetophotovoltaic Effect in Folded Graphene, *Phys. Rev. Lett.* **111**, 046601 (2013).
- [14] M. O. Goerbig, Electronic properties of graphene in a strong magnetic field, *Rev. Mod. Phys.* **83**, 1193 (2011).
- [15] J. Sonntag, A. Kurzmann, M. Geller, F. Queisser, A. Lorke, and R. Schützhold, Giant magneto-photoelectric effect in suspended graphene, *New J. Phys.* **19**, 063028 (2017).
- [16] N. M. R. Peres and T. Stauber, Transport in a clean graphene sheet at finite temperature and frequency, *Intl. J. Mod. Phys. B* **22**, 2529 (2008).
- [17] G. L. Klimchitskaya and V. M. Mostepanenko, Conductivity of pure graphene: Theoretical approach using the polarization tensor, *Phys. Rev. B* **93**, 245419 (2016).
- [18] K. F. Mak, M. Y. Sfeir, Y. Wu, C. H. Lui, J. A. Misewich, and T. F. Heinz, Measurement of the Optical Conductivity of Graphene, *Phys. Rev. Lett.* **101**, 196405 (2008).
- [19] K. J. Tielrooij, J. C. W. Song, S. A. Jensen, A. Centeno, A. Pesquera, A. Zurutuza Elorza, M. Bonn, L. S. Levitov, and F. H. L. Koppens, Photoexcitation cascade and multiple hot-carrier generation in graphene, *Nat. Phys.* **9**, 248 (2013).
- [20] T. Plötzing, T. Winzer, E. Malic, D. Neumaier, A. Knorr, and H. Kurz, Experimental verification of carrier multiplication in graphene, *Nano Lett.* **14**, 5371 (2014).
- [21] M. Mittendorff, F. Wendler, E. Malic, A. Knorr, M. Orlita, M. Potemski, C. Berger, W. A. de Herr, H. Schneider, M. Helm, and S. Winnerl, Carrier dynamics in Landau-quantized graphene featuring strong Auger scattering *Nat. Phys.* **11**, 75 (2015).
- [22] D. Brida, A. Tomadin, C. Manzoni, Y. J. Kim, A. Lombardo, S. Milana, R. R. Nair, K. S. Novoselov, A. C. Ferrari, G. Cerullo, and M. Polini, Ultrafast collinear scattering and carrier multiplication in graphene, *Nat. Commun.* **4**, 1987 (2013).
- [23] V. P. Gusynin and S. G. Sharapov, Transport of Dirac quasiparticles in graphene: Hall and optical conductivities, *Phys. Rev. B* **73**, 245411 (2006).
- [24] V. P. Gusynin, S. G. Sharapov, and J. P. Carbotte, Magneto-optical conductivity in graphene, *J. Phys.: Condens. Matter* **19**, 026222 (2007).
- [25] C. H. Lewenkopf, E. R. Mucciolo, and A. H. Castro Neto, Numerical studies of conductivity and Fano factor in disordered graphene, *Phys. Rev. B* **77**, 081410(R) (2008).
- [26] J. Liu, A. R. Wright, C. Zhang, and Z. Ma, Strong terahertz conductance of graphene nanoribbons under a magnetic field, *Appl. Phys. Lett.* **93**, 041106 (2008).
- [27] F. M. D. Pellegrino, G. G. N. Angilella, and R. Pucci, Strain effect on the optical conductivity of graphene, *Phys. Rev. B* **81**, 035411 (2010).
- [28] L. M. Zhang, Z. Q. Li, D. N. Basov, M. M. Fogler, Z. Hao, and M. C. Martin, Determination of the electronic structure of bilayer graphene from infrared spectroscopy, *Phys. Rev. B* **78**, 235408 (2008).
- [29] T. Winzer and E. Malic, Impact of Auger processes on carrier dynamics in graphene, *Phys. Rev. B* **85**, 241404(R) (2012).
- [30] E. Malic, T. Winzer, F. Wendler, and A. Knorr, Review on carrier multiplication in graphene, *Phys. Status Solidi B* **253**, 2303 (2016).
- [31] J. C. W. Song, K. J. Tielrooij, F. H. L. Koppens, and L. S. Levitov, Photoexcited carrier dynamics and impact-excitation cascade in graphene, *Phys. Rev. B* **87**, 155429 (2013).
- [32] T. Ando, Theory of electronic states and transport in carbon nanotubes, *J. Phys. Soc. Jpn.* **74**, 777 (2005).
- [33] L. Brey and H. A. Fertig, Edge states and the quantized Hall effect in graphene, *Phys. Rev. B* **73**, 195408 (2006).
- [34] K. Nakada, M. Fujita, G. Dresselhaus, and M. S. Dresselhaus, Edge state in graphene ribbons: Nanometer size effect and edge shape dependence, *Phys. Rev. B* **54**, 17954 (1996).
- [35] R. Kubo, Statistical-mechanical theory of irreversible processes. I. General theory and simple applications to magnetic and conduction problems, *J. Phys. Soc. Jpn.* **12**, 570 (1957).
- [36] G. D. Mahan, *Many Particle Physics* (Springer, New York, 1990).
- [37] J. Annett and G. L. W. Cross, Self-assembly of graphene ribbons by spontaneous self-tearing and peeling from a substrate, *Nature (London)* **535**, 271 (2016).
- [38] S. Cranford, D. Sen, and M. J. Buehler, Meso-origami: Folding multilayer graphene sheets, *Appl. Phys. Lett.* **95**, 123121 (2009).
- [39] H. C. Schniepp, K. N. Kudin, J.-L. Li, R. K. Prud'homme, R. Car, D. A. Saville, and I. A. Aksay, Bending properties of single functionalized graphene sheets probed by atomic force microscopy, *ACS Nano* **2**, 2577 (2008).
- [40] S. Park and H.-S. Sim, Magnetic edge states in graphene in nonuniform magnetic fields, *Phys. Rev. B* **77**, 075433 (2008).
- [41] D. A. Abanin, P. A. Lee, and L. S. Levitov, Charge and spin transport at the quantum Hall edge of graphene *Solid State Commun.* **143**, 77 (2007).
- [42] I. Romanovsky, C. Yannouleas, and U. Landman, Unique nature of the lowest Landau level in finite graphene samples with zigzag edges: Dirac electrons with mixed bulk-edge character, *Phys. Rev. B* **83**, 045421 (2011).
- [43] A. Tomadin, D. Brida, G. Cerullo, A. C. Ferrari, and M. Polini, Nonequilibrium dynamics of photoexcited electrons in graphene: Collinear scattering, Auger processes, and the impact of screening, *Phys. Rev. B* **88**, 035430 (2013).
- [44] T. Winzer, A. Knorr, and E. Malic, Carrier multiplication in graphene, *Nano Lett.* **10**, 4839 (2010).
- [45] F. Wendler, A. Knorr, and E. Malic, Carrier multiplication in graphene under Landau quantization, *Nat. Commun.* **5**, 3703 (2014).
- [46] E. Malic, T. Winzer, E. Bobkin, and A. Knorr, Microscopic theory of absorption and ultrafast many-particle kinetics in graphene, *Phys. Rev. B* **84**, 205406 (2011).
- [47] T. Ando, Screening effect and impurity scattering in monolayer graphene, *J. Phys. Soc. Jpn.* **75**, 074716 (2006).

- [48] E. H. Hwang and S. Das Sarma, Dielectric function, screening, and plasmons in two-dimensional graphene, *Phys. Rev. B* **75**, 205418 (2007).
- [49] S. M. Badalyan and F. M. Peeters, Effect of nonhomogeneous dielectric background on the plasmon modes in graphene double-layer structures at finite temperatures, *Phys. Rev. B* **85**, 195444 (2012).
- [50] J. P. Reed, B. Uchoa, Y. Il Joe, Y. Gan, D. Casa, E. Fradkin, and P. Abbamonte, The effective fine structure constant of freestanding graphene measured in graphite, *Science* **330**, 805 (2010).
- [51] D. M. Basko, and I. L. Aleiner, Interplay of Coulomb and electron-phonon interactions in graphene, *Phys. Rev. B* **77**, 041409(R) (2008).
- [52] A. C. Ferrari, J. C. Meyer, V. Scardaci *et al.*, Raman Spectrum of Graphene and Graphene Layers, *Phys. Rev. Lett.* **97**, 187401 (2006).
- [53] J. Yan, Y. Zhang, P. Kim, and A. Pinczuk, Electric Field Effect Tuning of Electron-Phonon Coupling in Graphene, *Phys. Rev. Lett.* **98**, 166802 (2007).
- [54] M. O. Goerbig, J.-N. Fuchs, K. Kechedzhi, and V. I. Fal'ko, Filling-Factor-Dependent Magnetophonon Resonance in Graphene, *Phys. Rev. Lett.* **99**, 087402 (2007).
- [55] T. Ando, Magnetic Oscillation of Optical Phonon in Graphene, *J. Phys. Soc. Jpn.* **76**, 024712 (2007).
- [56] F. Rana, Electron-hole generation and recombination rates for Coulomb scattering in graphene, *Phys. Rev. B* **76**, 155431 (2007).